Available online at www.sciencedirect.com

SciVerse ScienceDirect

journal homepage: www.elsevier.com/locate/jmbbm

Research paper

Towards a biomimetism of abdominal healthy and aneurysmal arterial tissues

L. Bailly [a,b,c,*], C. Geindreau [a], L. Orgéas [a], V. Deplano [b,c]

[a] CNRS/Université Joseph Fourier - Grenoble 1/Grenoble INP, Laboratoire Sols Solides Structures Risques (3SR Lab), 38041, Grenoble, France
[b] CNRS, IRPHE, 13384, Marseille, France
[c] Aix-Marseille Univ, IRPHE, 13384, Marseille, France

ARTICLE INFO

ABSTRACT

The aim of this work is to develop a new hyperelastic and anisotropic material mimicking histological and mechanical features of healthy and aneurysmal arterial tissues. The material is constituted by rhombic periodic lattices of hyperelastic fibres embedded into a soft elastomer membrane. To fit bi-axial experimental data obtained from the literature, with normal or pathologic human abdominal aortic tissues, the microstructure of the periodic lattices (fibre length, angle between fibres) together with the mechanical behaviour of the fibres (fibre tension-elongation curve) were optimised by using theoretical results arising from a multi-scale homogenisation process. It is shown that (i) a material constituted by only one periodic lattice of fibres is clearly not sufficient to describe all the experimental data set, (ii) a quantitative agreement between measurements and theoretical predictions is obtained by using a material with two fibre lattices, (iii) the optimised microstructures and mechanical properties of the fibrous lattices are strongly different for the abdominal healthy and aneurysmal arterial tissues, (iv) the anisotropic mechanical behaviour of the optimised material is described by only five parameters and (v) the optimal angles between fibres in the case of the healthy aorta are consistent with histological data. Several technical solutions of fibres can be considered as relevant candidates: this is illustrated in the particular cases of straight and wavy fibres.

© 2012 Elsevier Ltd. All rights reserved.

1. Motivations and objective

Abdominal aortic aneurysm (AAA) is a permanent dilatation of the abdominal aorta (AA), due to both biological and mechanical factors. Periodic hemodynamic forces applied to the arterial wall contribute to its gradual expansion and progressive degradation of its mechanical and structural properties. The ultimate consequence of this degradation is the aneurysm rupture. Current criteria commonly used for AAA rupture risk prediction derive from statistical observations, and rely on morphological configurations. Treatment is currently recommended for AAAs exceeding 5 cm in maximal diameter and those with expansion rates superior to 0.5 cm/year. Yet, these criteria are often neither easy to apply, nor always conclusive. Therefore, practicians are still awaiting new reliable criteria to predict

the aneurysmal expansion rate, determine its critical size at the point of rupture, and decide on a preventive AAA (endo) surgical repair (Vorp and Geest, 2005).

To this end, fundamental knowledge of the biomechanical behaviour of AAAs during pathogenesis, growth, and rupture is required. More specifically, a precise characterisation of fluid structure interactions in this biological context is needed, taking into account the 3D geometry of AAAs and the mechanical properties of aortic tissue. Therefore, during recent decades, numerous experimental, theoretical and computational works have been performed to predict the spatio-temporal evolutions of wall shear stresses and wall stresses induced by hemodynamic forces (Lasheras, 2007; Humphrey and Taylor, 2008). The majority of these works have focused on computational approaches, in particular finite-element analysis using idealised or patient specific AAA geometry, combined with isotropic (Thubrikar et al., 2001; Wolters et al., 2005; Raghavan et al., 2006; Scotti and Finol, 2007; Kleinstreuer et al., 2007) or anisotropic material models (Rodriguez et al., 2008; Vande Geest et al., 2008; Rissland et al., 2009; Toungara et al., 2012). By contrast, however, there is a huge disproportion of experimental devices suitable to assess and validate these numerical simulations. Despite current advances in medical imaging, *in vivo* experiments still remain highly delicate and not always relevant in quantifying fluid structure interactions. So far, most *in vitro* experiments have been performed on rigid (a)symmetric models of AAA (Egelhoff et al., 1999; Chong and How, 2004; Salsac et al., 2006). First experimental studies based on deformable models of AAA have been carried out recently (Deplano et al., 2007; Doyle et al., 2010). Experiments performed by Deplano et al. (2007) clearly highlight the impact of wall compliance on the dynamics of vortices within the AAA, and so, on the pressure distribution and wall shear stresses. However, current *in vitro* AAA models are constructed using elastomers with isotropic material properties, which are very far from the anisotropic hyperelastic behaviour of AAA tissues (Vande Geest et al., 2006). In recent decades, different materials, such as Dacron, expanded polytetrafluoroethylene (ePTFE) or electrospun biodegradable matrix (Jacobs et al., 2003; Chakfe et al., 2004; VanLieshout et al., 2006; Boland et al., 2004; McClure et al., 2010) have been developed in order to replace native arterial tissues. However, the mechanical behaviour of such materials (stiffness, anisotropy...) still remains quite far from those of healthy or pathologic arteries.

Therefore, in order to (i) design and process a material able to mimic the anisotropic hyperelastic properties of AA and AAA tissues and (ii) perform *in vitro* experiments similar to those carried out in Deplano et al. (2007) with more relevant models of AA and AAA, the aim of the present study is to provide a theoretical and numerical framework able to predict the microstructure and mechanical behaviour of this material. The chosen target is constituted by one or two periodic lattices of fibres embedded in a soft elastomer membrane, following the assumptions and material requirements presented in Section 2. The adopted methodology relies on a multi-scale homogenisation technique coupled with an optimisation process of the lattices detailed in Sections 2.2 and 2.3. Section 3 details the homogenised and optimised microstructures of the

periodic lattices (fibre lengths and angles between fibres) and mechanical behaviour of the fibres (tension–elongation curves), in order to fit the mechanical behaviour of healthy and pathologic human abdominal aortic tissues. Finally, Section 4 draws conclusions about the fibrous lattices to be designed, and points out the main challenges concerning the manufacturing of the new composite material.

2. Methodology

2.1. Biological material and target

2.1.1. Histological properties of the aortic tissue
Human abdominal aortic tissue is a complex cylindrical soft sandwich structure, architectured in three different concentric layers: the *intima* (innermost layer), the *media* (middle layer), and the *adventitia* (outer layer). Each layer is characterised by specific histological features, with different associated mechanical properties (Humphrey and Na, 2002; Holzapfel et al., 2002). The *intima* is composed of endothelial cells arranged in a thin layer of conjunctive tissue. The *media* is constituted by a three-dimensional network of smooth muscle cells, elastin and collagen fibrils with extracellular matrix. The *adventitia* mainly consists of fibroblasts, fibrocytes and collagen fibres. Within these layers, the distribution and arrangement of all components display a double-helix fibrous architecture, more or less equilibrated and characterised by distinctive fibre orientation (Holzapfel, 2006; Horny et al., 2010). Typically, the mean angle of such fibrous structures with respect to the orthoradial direction of the artery $\mathbf{e}_\theta$ is about 20°, 38° and 59° in *intimal*, *medial* and *adventitial* strips (Holzapfel, 2006; Horny et al., 2010). Moreover, at rest, it is interesting to note that these fibrous structures are arranged in a wavy architecture (Wolinsky and Glagov, 1964; Dobrin, 1978; Holzapfel, 2008).

2.1.2. Macroscopic mechanical behaviour of the aortic tissue
Previous tensile tests carried out on excised aortic specimens have evidenced the highly non-linear and anisotropic mechanical behaviour of human AA and AAA (Valenta, 1993; He and Roach, 1994; Raghavan et al., 1996; Thubrikar et al., 2001; Vande Geest et al., 2004, 2006). For the sake of simplicity, this behaviour is usually considered as essentially hyperelastic, the non-linearity of which is ascribed to the particular wavy architecture of the fibrous structures, which tend to straighten along the loading direction when they are subjected to a mechanical loading (Wolinsky and Glagov, 1964; Dobrin, 1978; Holzapfel, 2008): this gives the arterial tissues a macroscopic mechanical response exhibiting a typical J-shape (see below). Moreover, the preferred orientations of the fibrous architecture are responsible for the mechanical anisotropy of the arterial tissues.

In the present study, measurements performed by Vande Geest et al. (2006) have been chosen as a reference to identify AA and AAA biomechanical behaviour at the macroscale. In these experiments, the authors investigated the bi-axial biomechanical response of square AA and AAA tissue
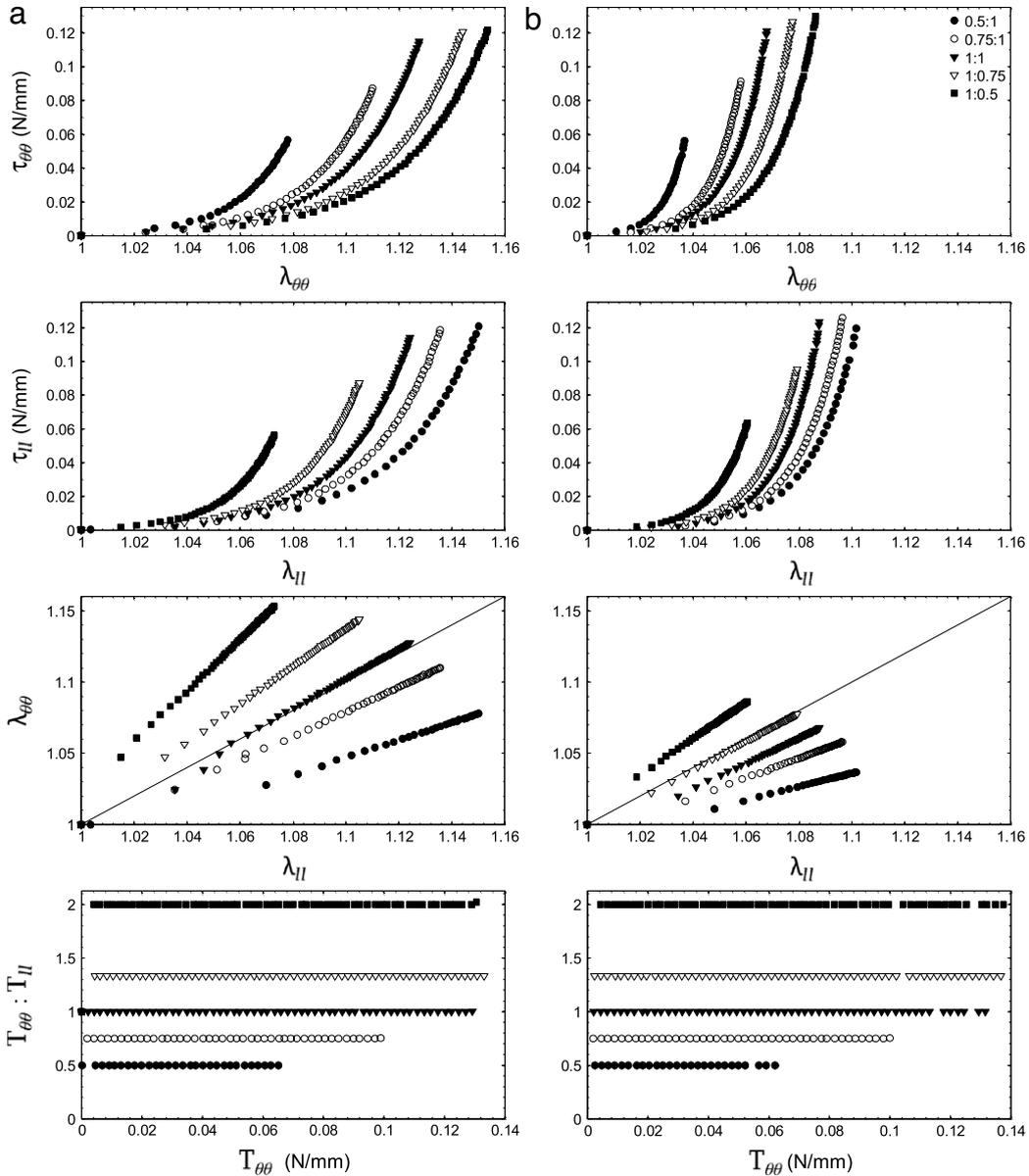
Fig. 1 – Average experimental data sets chosen as reference for (a) AA and (b) AAA macroscopic mechanical behaviour.
(From top to bottom) **Cauchy tension** τ **versus elongation, corresponding elongation paths** $(\lambda_{ll}, \lambda_{\theta\theta})$ **and axial Piola–Kirchhoff tension ratio** $T_{\theta\theta} : T_{ll}$**. The legend in the upper-right panel refers to the ratio** $T_{\theta\theta} : T_{ll}$**.**
Source: **From Vande Geest et al., 2006.**

samples (8 AA samples and 26 AAA samples) to planar bi-axial loadings along the orthoradial $\mathbf{e}_\theta$ and longitudinal $\mathbf{e}_l$ directions. The initial gauge width of the tested specimen was $L_0 = 20$ mm, whereas the average thicknesses e_0 of the AA and AAA specimens were equal to 1.49 mm and to 1.32 mm, respectively. During the tests, the orthoradial and longitunal forces and elongations were measured, i.e. F_θ, F_l and $\lambda_{\theta\theta}, \lambda_{ll}$, respectively. Tests were made at constant tension ratios $T_{\theta\theta}/T_{ll}$, where the components $T_{\theta\theta}$ and T_{ll} of the first Piola–Kirchhoff tension tensor $\mathbf{T}$, respectively along the orthoradial and longitudinal directions, are defined as F_θ/L_0 and F_l/L_0. Various tension ratios $T_{\theta\theta}/T_{ll}$ were studied, i.e. 0.5:1, 0.75:1, 1:1, 1:0.75 and 1:0.5, the tests being stopped when the highest tension reached 120 N m^{-1}. Results are

summarised in Fig. 1. In particular, the first four graphs of this figure give the evolution of the components $\tau_{\theta\theta}$ and τ_{ll} of the averaged Cauchy tension tensor τ as functions of $\lambda_{\theta\theta}, \lambda_{ll}$ for the AA and AAA specimens. They clearly emphasise the non-linear response of the arterial tissues. They also show that AAA tissues are much stiffer than AA tissues: whatever the considered tested tension ratio, their J-shape responses stiffen at lower elongations than those recorded for the AA tissues. Also, the elongation paths $(\lambda_{\theta\theta}, \lambda_{ll})$ plotted in the next two graphs tend to prove that the anisotropy of the AAA tissues is more pronounced: the elongation paths do not exhibit a symmetry with respect to the 1:1 path (dotted line in Fig. 1), so that AAA tissue are stiffer in the orthoradial direction than in the longitudinal direction.
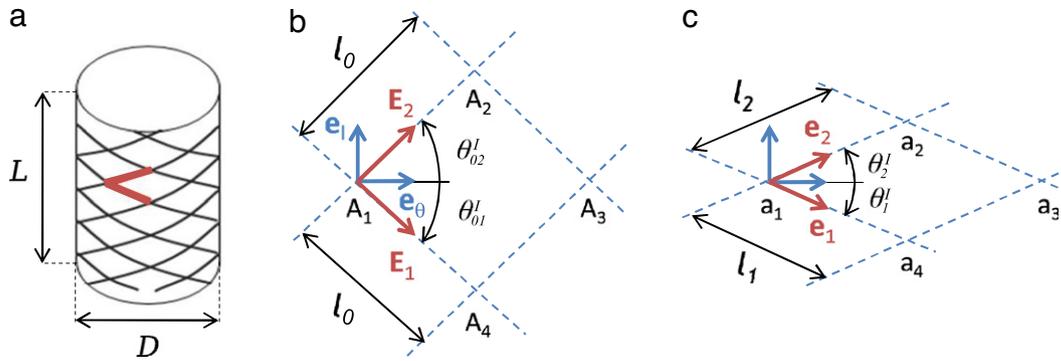
Fig. 2 – (a) Typical rhombic lattice under consideration and corresponding periodic Representative Elementary Volume of the *one-layer fibrous structure* solution: (b) initial undeformed configuration $\mathcal{C}_0$, (c) actual configuration $\mathcal{C}$.

2.1.3. Geometry and mechanics of the target material at the microscale

In an attempt to mimic the macroscopic hyperelastic and anisotropic mechanical properties of the arterial tissues emphasised from Fig. 1, by taking into account the histological features of these biological materials, we propose to design a target composite material composed of a thin and soft hyperelastic membrane reinforced by simplified periodic fibrous microstructures displaying preferred orientations. Two basic solutions are envisaged:

- The first solution is sketched in Fig. 2(a). The composite is characterised by a *one-layer fibrous structure* comprising a single lattice *I* of crossed and identical continuous fibres embedded into a soft elastomer matrix.
- The second solution is characterised by a *bi-layers fibrous structure* made up of two parallel fibrous lattices *I* and *II* embedded into the soft matrix.

As shown for example in Fig. 2(a) in the case of the *one-layer fibrous structure*, each fibrous lattice can be seen as a repetition of a Representative Elementary Cell (REC) lying in the $(\mathbf{e}_\theta, \mathbf{e}_l)$ plane and sketched in Fig. 2(b) and (c) in the initial $\mathcal{C}_0$ and deformed $\mathcal{C}$ configurations, respectively. The following points summarise the main microscale geometrical and mechanical hypotheses associated with this REC:

(1) The REC displays a rhomb shape and it is characterised by two periodicity vectors $\mathbf{P}_1 = \mathbf{A_1A_4} = l_0\mathbf{E}_1$ and $\mathbf{P}_2 = \mathbf{A_1A_2} = l_0\mathbf{E}_2$ (resp. $\mathbf{p}_1 = \mathbf{a_1a_4} = l_1\mathbf{e}_1$ and $\mathbf{p}_2 = \mathbf{a_1a_2} = l_2\mathbf{e}_2$) joining the extremities A_1, A_2 and A_4 (resp. a_1, a_2 and a_4) of the REC in the initial (resp. deformed) configuration. The REC's surface is noted $S_0^{REC} = \|\mathbf{P}_1 \times \mathbf{P}_2\|$ (resp. $S^{REC} = \|\mathbf{p}_1 \times \mathbf{p}_2\|$) in $\mathcal{C}_0$ (resp. in $\mathcal{C}$). The angles $(\mathbf{e}_\theta, \mathbf{P}_1)$ and $(\mathbf{e}_\theta, \mathbf{P}_2)$ (resp. $(\mathbf{e}_\theta, \mathbf{p}_1)$ and $(\mathbf{e}_\theta, \mathbf{p}_2)$) are respectively noted θ_{01}^I and θ_{02}^I (resp. θ_1^I and θ_2^I) in $\mathcal{C}_0$ (resp. in $\mathcal{C}$). In the initial configuration $\mathcal{C}_0$, we suppose that: $\theta_{02}^I = -\theta_{01}^I$.
(2) Fibres are supposed to be linked at the REC extremities A_1, A_2, A_3 and A_4, in such a way that the relative displacement of fibres at these points is zero (their relative rotation may be free or constrained).
(3) In between these points, the geometry of the fibres is free. For example, fibres i (i = 1 and 2) can be straight fibres, so that their initial and deformed lengths are expressed

as $l_{0i}^f = \|\mathbf{P}_i\| = l_0$ and $l_i^f = \|\mathbf{p}_i\| = l_i$, respectively. Fibres i can also exhibit a wavy shape. In that case $\|\mathbf{P}_i\| = l_0$ (resp. $\|\mathbf{p}_i\| = l_i$) represents their initial (resp. actual) chord, which is linked with their initial (resp. actual) length l_{0i}^f by $l_{0i}^f = \xi_{0i}l_0$ (resp. $l_i^f = \xi_i l_i$), ξ_{0i} (resp. ξ_i) being the initial (resp. the actual) tortuosity of fibre i.

(4) Similarly, in between these points, the mechanical behaviour of the fibres, *i.e.* the relations between the fibre tensions $\mathbf{t}_i = t_i\mathbf{e}_i$ (no summation on the indice i) and the elongations of their corresponding chords $\lambda_i = l_i/l_0$, are supposed to be of hyperelastic types, *i.e.* the t_i's can be ascribed a strain energy which is a function of the λ_i's. In order to mimic the J-shape curves observed during the tension of collagen fibres, various functions can be used (Holzapfel et al., 2000; Freed et al., 2005; Volokh, 2008). Here, a phenomenological model was chosen, rather close to the one proposed in Freed et al. (2005) so that:

$$\mathbf{t}_i = c_0\lambda_i\left[e^{0.5c_1((\lambda_i)^2-1)} - 1\right]\mathbf{e}_i, \tag{1}$$

where the c_i's are two constitutive parameters.

(5) The mechanical contribution of the thin elastomer membrane, of initial and actual thickness e_0^m and e^m, is described by a simple neo-Hookean model, thus characterised by a volumetric strain-energy function $W^m = c^m(I_1 - 3)/2$, where c^m is a positive material parameter and where $I_1 = \text{tr}(\mathbf{C})$ denotes the first principal invariant of the right Cauchy–Green tensor. Let us remark that other more sophisticated hyperelastic models could have been used, without modifying the method presented here.

(6) For the sake of simplicity, the same type of fibre (geometry and mechanical behaviour) is chosen for the *one-layer* and the *bi-layers fibrous structures*. Besides, the second lattice *II* of the *bi-layers fibrous structure* is supposed to be identical to its first lattice *I*, except their initial orientation angles θ_0^I and θ_0^{II}, which can be different (notice that associated vectors such as the $\mathbf{P}_i, \mathbf{p}_i, \mathbf{E}_i$ and $\mathbf{e}_i$ with (i = 1, 2) must also be adjusted accordingly).

(7) The mechanical interactions between the homogenous elastomer membrane and the fibrous lattice(s), but also between the fibres of the REC during their relative rotations, are assumed to be negligible.

2.2. Homogenisation

According to the last hypothesis, the mechanical behaviour of the considered composite material can be roughly considered as the sum of two (or three) contributions, i.e. (i) that induced by the deformation of the thin isotropic incompressible homogeneous membrane of constant initial thickness, and (ii) those induced by the deformation of the fibrous lattices. Such contributions arise when the composite is subjected to a 2D transformation gradient $\mathbf{F}$ in the $(\mathbf{e}_\theta, \mathbf{e}_l)$ plane. Hence, the overall macroscopic Cauchy tension tensor τ of the composite material can be written as:

$$\tau^c = \tau^m + \tau^I + \tau^{II}, \tag{2}$$

where τ^m stands for the tension of the elastomer membrane, and where τ^I and τ^{II} are the contributions of the fibre lattices (for the *one layer* solution, the last term vanishes):

- The tension τ^m is function of the material parameter c^m and the instantaneous thickness e^m. It can be written as:

$$\tau^m = e^m \left(-p\delta + 2\mathbf{F}\frac{\partial W^m}{\partial I_1}\mathbf{F}^T \right), \tag{3}$$

where p represents a contribution to hydrostatic stress. In the particular bi-axial deformation studied in this work, the last expression becomes, by noting $\tilde{c}^m = c^m e_0^m$:

$$\tau^m = \frac{\tilde{c}^m}{\lambda_{\theta\theta}\lambda_{ll}} \left[(\lambda_{\theta\theta}^2 - \lambda_{\theta\theta}^{-2}\lambda_{ll}^{-2})\mathbf{e}_\theta \otimes \mathbf{e}_\theta \right.$$
$$\left. + (\lambda_{ll}^2 - \lambda_{\theta\theta}^{-2}\lambda_{ll}^{-2})\mathbf{e}_l \otimes \mathbf{e}_l \right]. \tag{4}$$

- By using the homogenisation of periodic discrete structures (Tollenaere and Caillerie, 1998; Boutin and Hans, 2003; Le Corre et al., 2004; Caillerie et al., 2006), it is possible to obtain suitable analytical forms for the tension contributions τ^I and τ^{II} (Caillerie et al., 2006). Indeed, conclusions drawn from the work of Caillerie et al. prove that the considered discrete fibrous networks behave macroscopically as standard hyperelastic continua. The discrete homogenisation also provides self equilibria to be solved on REC, in order to estimate the effective hyperelastic properties of the continua at the macroscale. In the case of the simple REC considered in this work, it is possible to solve analytically such self equilibria, and to show that the motions of the extremities A_i of the REC are affine functions of the macroscopic transformation gradient $\mathbf{F}$. Moreover, the homogenisation provides analytical expressions of the macroscopic Cauchy tension tensors τ^I and τ^{II}. For example, τ^I can be expressed as:

$$\tau^I = \frac{1}{\|\mathbf{p}_1 \times \mathbf{p}_2\|}(\mathbf{t}_1 \otimes \mathbf{p}_1 + \mathbf{t}_2 \otimes \mathbf{p}_2). \tag{5}$$

A similar expression is obtained for τ^{II}. Obviously, this homogenisation process is valid if the condition of separation of scale is fulfilled, i.e. $l_0 \ll D$ or L, where D and L are the typical characteristic lengths of the artery (Fig. 2). Finally, note that in the particular bi-axial loadings studied in this work, in the deformed configuration $\mathcal{C}$ the angles θ_i^I, the lengths l_i and, thus, the elongations and tensions λ_i and t_i do not depend on the fibre i, i.e. $\theta_1^I = -\theta_2^I = -\theta^I, l_1 = l_2 = l, \lambda_1 = \lambda_2 = \lambda$ and $t_1 = t_2 = t$. Thus, by noting

$\tilde{t}(\lambda) = t(\lambda)/l$, Eq. (5) can be simplified to:

$$\tau^I = \frac{\tilde{t}}{\sin 2\theta^I}(\mathbf{e}_1 \otimes \mathbf{e}_1 + \mathbf{e}_2 \otimes \mathbf{e}_2). \tag{6}$$

Finally, for a given macroscopic elongation path $(\lambda_{\theta\theta}, \lambda_{ll})$, the mechanical behaviour of the *one-layer composite* can be deduced from (2) combined with (4) and (6), and depends on only four constitutive parameters to determine: three of them relate to the fibrous lattice at the initial unloaded state $(\theta_0^I, \tilde{c}_0 = c_0/l_0, c_1)$ and one of them relates to the elastomer membrane $\tilde{c}^m = c^m e_0^m$. For the *bi-layers composite*, only one additional constitutive parameter is required, i.e. the angle θ_0^{II}.

2.3. Optimisation of microstructure

In order to determine the microstructural parameters of all target solutions and to mimic the mechanical behaviour of AA and AAA samples, an optimisation process has been applied to fit previous analytical predictions with bi-axial experimental data displayed in Fig. 1. Thus, the following route has been taken:

(i) The different experimental elongation paths $(\lambda_{\theta\theta}, \lambda_{ll})$ obtained by Vande Geest et al. (2006) and displayed in Fig. 1 have been considered as inputs. Also, in order to limit the number of available solutions, the constitutive parameter $\tilde{c}^m$ was arbitrarily fixed to 0.014 MPa mm. Such a value typically corresponds to that of an unfilled silicone membrane of initial thickness e_0^m of $\approx$0.2 mm.

(ii) The unknown constitutive parameters to be determined were the angles $\theta_0^I, \theta_0^{II}$ (only for the bi-layers solution), together with the fibre constant $\tilde{c}_0$ and c_1, both being required to determine the mechanical behaviour and the chord length l_0 of the fibres.

(iii) A least-squares approach has been employed to minimise the sum of errors $Error_k$ ($k = [1..5]$) with respect to the model's parameters, k referring to a specific macroscopic loading. The error of the homogenised predictions for each loading condition k was given as:

$$Error_k = \sum_{j=1}^n \left[(\tau_{ll} - \tau_{ll}^c)_j^2 + (\tau_{\theta\theta} - \tau_{\theta\theta}^c)_j^2 \right], \tag{7}$$

where n is the number of experimental points considered in the specified kth data sets ($n = 15$), τ_{ll} and $\tau_{\theta\theta}$ the experimental longitudinal and orthoradial Cauchy tensions (see Fig. 1), and τ_{ll}^c and $\tau_{\theta\theta}^c$ the longitudinal and orthoradial Cauchy tensions in the composite membranes (see Eqs. (2), (4) and (6)). The global error of the model $Error_{model}$ was calculated as the sum of the five scalars $Error_k$, thus defined as a non-linear function of parameters $(\theta_0^I, \tilde{c}_0, c_1)$ (resp. $(\theta_0^I, \theta_0^{II}, \tilde{c}_0, c_1)$) in the one-layer (resp. bi-layers) solution. Minimisation of the multi-variable function $Error_{model}$ was achieved using a non-linear constraint optimisation process relying on the Matlab routine *fmincon* (optimisation Toolbox), a gradient-based method allowing one to define lower and upper bounds on each parameter. An interior-point algorithm was optionally selected (Byrd et al., 2000; Waltz et al., 2006). The optimisation was completed by using a termination tolerance of $1 \cdot 10^{-20}$ on the

objective function (*Tol.Fun*), the constraint violation (*Tol.Con*) and on the solution (*Tol.X*). The guarantee of convergence was evaluated by using the first-order optimality output, based on Karush–Kuhn–Tucker conditions (Kuhn and Tucker, 1951; Nocedal and Wright, 2006). Each optimisation was iterated by replacing the initialised with optimised parameters until stability of the converged solution. At the end of the optimisation process, the relative error ϵ_i between an experimental couple (λ_i, τ_i) and the corresponding optimised couple (λ_i^c, τ_i^c) can be calculated using:

$$\epsilon_i = \frac{[(\lambda_i^c - \lambda_i)^2 + (\tilde{\tau}_i^c - \tilde{\tau}_i)^2]^{0.5}}{[(\lambda_i - 1)^2 + \tilde{\tau}_i^2]^{0.5}}, \tag{8}$$

with $i \in [1, n]$, and where $\tilde{\tau}_i = \tau_i \frac{\max(\lambda_i - 1)}{\max(\tau_i)}$ and $\tilde{\tau}_i^c = \tau_i^c \frac{\max(\lambda_i^c - 1)}{\max(\tau_i^c)}$ are respectively defined as the normalised experimental and theoretical Cauchy tensions. In the following, the maximum and average relative errors are calculated by $\epsilon_{max} = \max_{i \in [1,n]} \epsilon_i$ and $\bar{\epsilon} = \frac{1}{n} \sum_{i=1}^{n} \epsilon_i$.

(iv) At last, having determined the optimal microstructure parameters (angles and tension $\tilde{t}(\lambda)$), the homogenised model can be inverted and conducted by imposing experimental Piola–Kirchhoff tensions ratio $T_{\theta\theta} : T_{ll}$ instead of the experimental elongation path $(\lambda_{\theta\theta}, \lambda_{ll})$. This step has been initiated as a validation of the method, aiming at mimicking the exact control conditions that were carried out by Vande Geest et al. (2006) during the measurements.

3. Results

The relevance of the two envisaged solutions has been tested with different assumptions. For that purpose, the optimisation of both targets' architecture are presented and compared.

3.1. One-layer target material

The one-layer target has been subjected to two optimisation procedures. Indeed, a first pilot procedure of *individual optimisation* has been conducted, in order to identify possible microstructure features which may be specific to each macroscopic loading path. Then, a *mean optimisation* procedure has been performed to determine the microstructure features necessary to mimic the aortic wall behaviour, whatever the considered loading path.

3.1.1. Individual optimisations

This pilot study allowed us to test the validity of the methodology and to characterise the mechanical response of the one-layer model stretched under a given elongation loading. For that purpose, the methodology detailed in Section 2.3 has been applied, with step (iii) modified such as minimisation only occurs on $Error_{model} = Error_k, k = [1..5]$ (no summation on the index k). Unknown parameters were initialised with an arbitrary fixed $\theta_0^I = 45°$, and with material constants $\tilde{c}_0$ and c_1 deduced by inversion of the homogenised

Table 1 – Relative error between optimised data and experimental data (Healthy aorta) depicted in Fig. 3, **mimicking elongation paths** $(\lambda_{ll}, \lambda_{\theta\theta})$ **(left), and mimicking tension ratios** $T_{\theta\theta} : T_{ll}$ **(right). Maximum value** ϵ_{max}, **mean value** $\bar{\epsilon}$. **All errors are in %, as defined in Eq.** (8).

		Imposed $(\lambda_{ll}, \lambda_{\theta\theta})$		Imposed $T_{\theta\theta} : T_{ll}$	
	$T_{\theta\theta} : T_{ll}$	ϵ_{max} (%)	$\bar{\epsilon}$ (%)	ϵ_{max} (%)	$\bar{\epsilon}$ (%)
	0.5:1	11.36	2.12	73.56	22.80
	0.75:1	3.56	0.89	33.48	8.54
$\theta\theta$	1:1	2.16	0.47	6.89	0.69
	1:0.75	1.82	0.50	9.14	3.27
	1:0.5	1.52	0.88	11.35	4.43
	0.5:1	1.34	0.76	13.11	5.52
	0.75:1	1.69	0.73	9.80	3.70
ll	1:1	2.14	0.47	6.91	0.71
	1:0.75	3.47	0.67	31.18	7.70
	1:0.5	6.26	1.50	81.32	24.33

model, imposing $\theta_0^I = 45°$. Likewise, lower and upper bounds defined on each parameter were initially chosen as follows: $\theta_0^I \in [1°; 90°]$, $\tilde{c}_0 \in [0; 0.01]$ N mm^{-1} and $c_1 \in [10; 100]$. Typical results of these individual optimisations are illustrated in Fig. 3 in the case of AA specimens. Important features can be highlighted by analysing the mechanical aspects at both macroscopic and microscopic scales.

- *Macroscopic scale*—Tension-elongation curves $\tau_{\theta\theta} - \lambda_{\theta\theta}$ and $\tau_{ll} - \lambda_{ll}$ plotted in Fig. 3 compare the predictions given by the above homogenisation model (2) with the data measured by Vande Geest et al. (2006). The elongation paths $(\lambda_{ll}, \lambda_{\theta\theta})$ and axial Piola–Kirchhoff tension ratios $T_{\theta\theta} : T_{ll}$ have also been reported. The figure compares the direct output of the optimisations obtained while imposing experimental elongation paths $(\lambda_{ll}, \lambda_{\theta\theta})$ (Fig. 3(a)) against the resimulated data obtained while imposing constant experimental tension ratios $T_{\theta\theta} : T_{ll}$ (Fig. 3(b)). For all five data series, values of the first-order optimality are less than $2 \cdot 10^{-6}$, indicating complete convergence. Yet, the results evidence that an *a priori* negligible discrepancy between the prediction and the measurement of the ratio $T_{\theta\theta} : T_{ll}$ can yield much larger errors in the estimation of tension–elongation responses and corresponding elongation path. As an example, when $k = 1$, the relative error ϵ_i obtained on curve $\tau_{\theta\theta} - \lambda_{\theta\theta}$ by mimicking experimental elongation paths, varies from 0.00% to 11.36% (mean value 2.12%). This error comprises between 0.00% and 75.56% (mean value 22.80%) by mimicking an experimental tension ratio $T_{\theta\theta} : T_{ll} = 0.5 : 1$. This trend is maintained for all data series k, in both orthoradial and longitudinal directions, as reported in Table 1. This remarkable error propagation is due to the high non-linearity of AA mechanical behaviour. Therefore, particular caution should be given to the comparison between *both* elongation and tension paths simulated by a model to be assessed. In this study, the relevance of the optimised data will be further evaluated exclusively within the experimental loading conditions, that is, by imposing a constant tension ratio $T_{\theta\theta} : T_{ll}$.

- *Microscopic scale*—Important microstructure features have been highlighted as a result of the preliminary optimisations. Fig. 4 displays the optimised mechanical behaviour
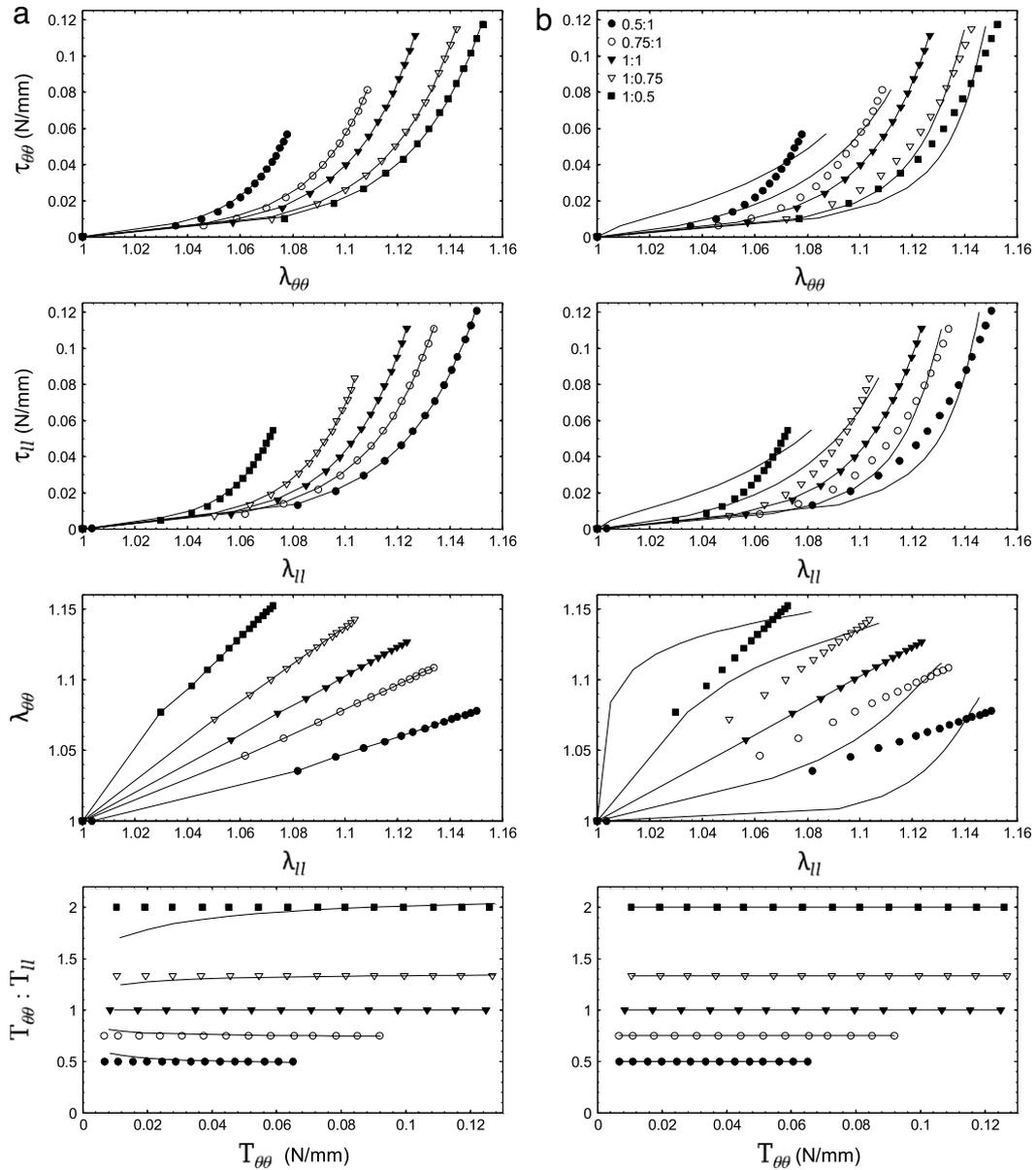
Fig. 3 – Comparison between the predictions of the *one-layer* model (solid lines) and Vande Geest experimental data (symbols) at the macroscale for healthy AA samples. Optimisation has been processed for each loading path individually. (a) Optimised data obtained while imposing experimental elongation paths $(\lambda_{\theta\theta}, \lambda_{ll})$. (b) Optimised data obtained while imposing experimental Piola–Kirchhoff tension ratios $T_{\theta\theta} : T_{ll}$.

Table 2 – Optimised microstructural parameters of the one-layer composite material, firstly calculated by individual optimisations, then by a mean optimisation process run on both extreme bi-axial loads 0.5:1 and 1:0.5.

$T_{\theta\theta} : T_{ll}$	Case AA			Case AAA		
	$\tilde{c}_0$ (N mm^{-1}) $\times 10^{-4}$	c_1 (−)	θ_0^I (°)	$\tilde{c}_0$ (N mm^{-1}) $\times 10^{-4}$	c_1 (−)	θ_0^I (°)
0.5:1	5.29	37.01	55	1.59	74.59	54
0.75:1	5.78	38.56	49	2.43	72.86	49
1:1	6.02	38.84	45	2.48	76.40	45
1:0.75	5.01	38.92	41	2.84	72.82	41
1:0.5	4.65	37.82	35	2.99	69.96	35
0.5:1 & 1:0.5	5.74	41.37	45	3.17	75.54	46

$\tilde{t}(\lambda)$ required to mimic AA (Fig. 4 *top*) and AAA (Fig. 4 *bottom*) for each loading path. Corresponding parameters $(\tilde{c}_0, c_1)$ to

each fibre exponential-shaped response are summarised in Table 2. For the two target composite membranes, it

is shown that the optimal hyperelastic behaviour of the constitutive fibres are quite similar, regardless of the ratio $T_{\theta\theta} : T_{ll}$. To analyse these results semi-quantively, an elastic modulus ($\tilde{E}_c$) and a critical elongation ($\tilde{\lambda}_c$) can be extracted from each $\tilde{t} - \lambda$ curve, as illustrated in Fig. 4. These values have been estimated for a given value of $\tilde{t} = 0.06$ N mm^{-1}. They allow one to characterise the linear response observed in the highest strains, as well as the elongation associated with the transition between low- and high-stiffness behaviour. In the healthy case, $\tilde{E}_c$ varies from 2.51 to 2.63 N mm^{-1} (mean value 2.58 N mm^{-1}), and $\tilde{\lambda}_c$ varies from 1.089 to 1.098 (mean value 1.094). In the pathological case, $\tilde{E}_c$ varies from 4.53 to 4.92 N mm^{-1} (mean value 4.73 N mm^{-1}), and $\tilde{\lambda}_c$ varies from 1.057 to 1.064 (mean value 1.060). Therefore, a stiffening of the microstructure is needed in the pathological case, characterised by an average modulus $\tilde{E}_c$ doubled compared to its value in healthy case.

As regards the fibre orientations in the one-layer model, the optimised initial angle θ_0^I varies from 35° to 55°, depending on the bi-axial loading conditions. Results are detailed in Table 2. For each mechanical loading, the optimal angle θ_0^I is of the same order of magnitude for the AA and AAA cases.

3.1.2. Mean optimisation

Here, a unique fibrous architecture is looked for, to check if the one-layer model is sufficient to reproduce the aortic macroscopic responses measured for several loading paths $T_{\theta\theta} : T_{ll}$. A typical example of the mean optimisation procedure has been applied on two ratios, so as to minimise the global error $Error_{model} = \sum_{k=1,5} Error_k$ (see (7)) within the scope of healthy samples. Microstructure parameters have been initialised by the triplet $(\tilde{c}_0, c_1, \theta_0^I)$, which was obtained by applying the previous individual optimisation to the case where $T_{\theta\theta} : T_{ll} = 0.5 : 1$ ($k = 1$) (see Table 2). The resulting optimised microstructure properties are listed in Table 2, along with those calculated by the individual procedures. Associated predictions at the macroscopic scale are displayed in Fig. 5. These results are unchanged if the optimisation is initialised by the triplet $(\tilde{c}_0, c_1, \theta_0^I)$ obtained in the case where $T_{\theta\theta} : T_{ll} = 1 : 0.5$ ($k = 5$).

Despite an achieved repeatable convergence (with an acceptable first-order optimality around $2 \cdot 10^{-6}$), a quantitative disagreement between experimental data and model predictions is observed for both series 1 and 5. Regarding data series $k = 1$, the relative error ϵ_i evaluated on tension–elongation curves varies from 255.5% to 317.2% (mean value 297.4%) in the orthoradial direction, and from 35.8% to 144.0% (mean value 128.9%) in the longitudinal direction. Similar discrepancies can be noticed for series $k = 5$, as well as for the pathological specimens. These results demonstrate that the one-layer model is not sufficient to mimic the AA and AAA mechanical responses measured in the most extreme bi-axial loads, and a fortiori in all other investigated loading paths.

3.2.   Bi-layer target material

Accounting for the limitations of the one-layer solution, the bi-layers solution is now studied. Here, a mean optimisation
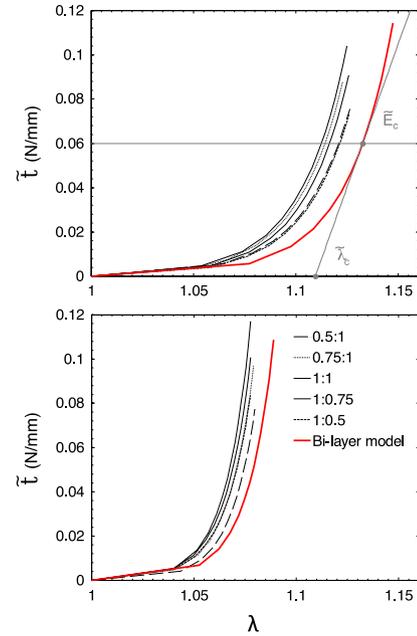
Fig. 4 – Optimised microscopic mechanical behaviour $\tilde{t} - \lambda$ predicted by the homogenised model, for healthy (*top*) and pathological (*bottom*) cases. Comparison between the *one-layer* model predictions (individual optimisations, *thin lines*), and the *bi-layer* model predictions (mean optimisation, *thick line*).

procedure has been adopted, by operating upon the five experimental bi-axial loads. The four unknown parameters $(\theta_0^I, \theta_0^{II}, \tilde{c}_0, c_1)$ were initialised according to the converged solutions of the above individual optimisations, run on the two extreme bi-axial loads in the one-layer solution. Therefore, initial angles θ_0^I and θ_0^{II} were respectively set to 35° and 55° in the healthy case and to 35° and 54° in the pathological case. The material constants $\tilde{c}_0$ and c_1 were initially fixed to values that correspond to the case where $T_{\theta\theta} : T_{ll} = 0.5 : 1$ or the case where $T_{\theta\theta} : T_{ll} = 1 : 0.5$ (see Table 2). Similarly, lower and upper bounds defined on each parameter were chosen in agreement with previous calculations: $\theta_0^I \in [1°; 44°]$, $\theta_0^{II} \in [46°; 90°]$, $\tilde{c}_0 \in [0; 0.1]$ N mm^{-1} and $c_1 \in [10; 100]$ in the AA case, $\tilde{c}_0 \in [0; 4\,10^{-4}]$ N mm^{-1} and $c_1 \in [60; 80]$ in the AAA case. Results that are revealed thereafter highlight a mechanical behaviour very different from the predictions of the one-layer solution, at both macroscopic and microscopic scales.

- *Macroscopic scale*— Fig. 6 displays the predictions of the *bi-layers solution* together with the reference experimental data for both AA and AAA specimens, in terms of tension–elongation curves ($\tau_{\theta\theta} - \lambda_{\theta\theta}, \tau_{ll} - \lambda_{ll}$), elongation paths ($\lambda_{ll}, \lambda_{\theta\theta}$) and Piola–Kirchhoff tension ratios $T_{\theta\theta} : T_{ll}$. The first-order optimality value amounts to $7 \cdot 10^{-6}$ in the AA case and $4 \cdot 10^{-6}$ in the AAA case. Whatever the considered tension component ($\tau_{\theta\theta}$ or τ_{ll}), this figure shows that the trends given by the proposed analytical model, despite its simplicity and bearing in mind that optimisation was run on only four constitutive parameters $(\theta_0^I, \theta_0^{II}, \tilde{c}_0, c_1)$, fit rather well to the experimental data as compared to the one-layer model predictions (see Fig. 5).
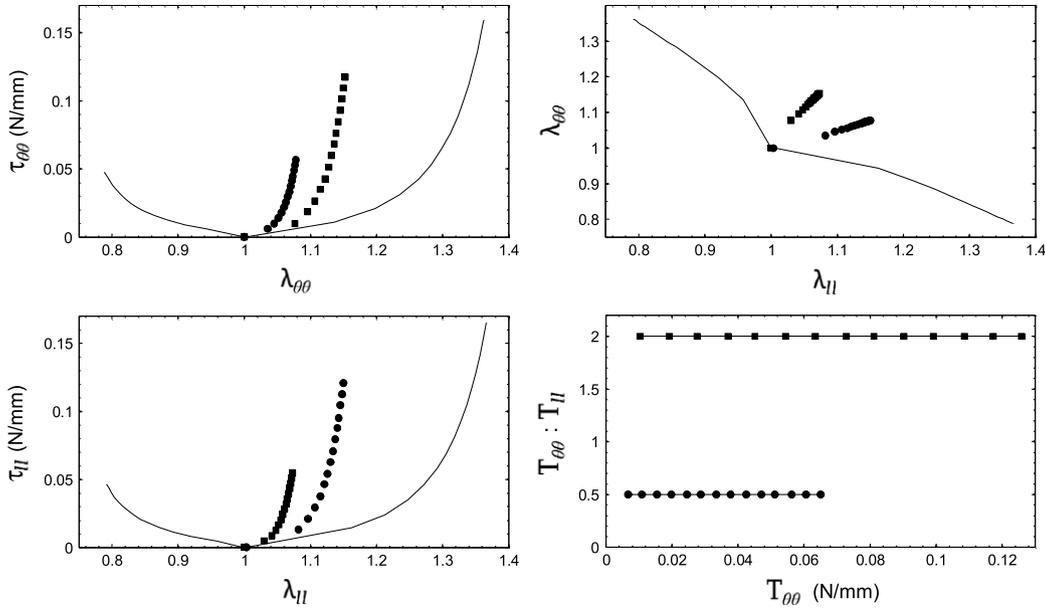
Fig. 5 – Comparison between the prediction of the *one-layer fibrous structure* model (*solid lines*) and Vande Geest experimental data (*symbols*) at the macroscale for healthy AA samples. Optimisation has been processed as an average on both extreme bi-axial loads ($T_{\theta\theta} : T_{ll} = 1 : 0.5$ and $0.5 : 1$). Optimised data have been obtained by imposing experimental tension ratios $T_{\theta\theta} : T_{ll}$.

Even if noticeable deviations still occur for extreme bi-axial loads, the average relative error $\bar{\epsilon}$ estimated in the AA case (resp. in the AAA case) varies from 1.44% to 18.88% (resp. 2.08% from to 28.75%) on curves $\tau_{\theta\theta} - \lambda_{\theta\theta}$, and from 1.16% to 21.78% on curves $\tau_{ll} - \lambda_{ll}$ (resp. 2.72% from to 10.67%). Details of the relative errors $\epsilon_{\max}$ and $\bar{\epsilon}$ matched to each experimental loading are listed in Table 3.

- *Microscopic scale*—The optimised microscopic mechanical behaviour $\tilde{t}(\lambda)$ is rather close to the microscopic responses deduced from individual optimisations previously carried out on the *one-layer* model, as illustrated in Fig. 4. A stiffening of the microstructure is still predicted in the pathological case but, compared to the *one-layer* solution, this stiffening is slightly weaker and occurs at slightly higher elongations: modulus $\tilde{E}_c$ goes from 2.59 N mm^{-1} in the AA case to 4.60 N mm^{-1} in the AAA case, whereas the critical stretch $\tilde{\lambda}_c$ drops from 1.109 to 1.068, respectively. Material parameters $(\tilde{c}_0, c_1)$ associated with each optimised exponential-shaped response are listed in Table 4, along with optimised fibre orientations θ_0^I and θ_0^{II}.

4. Discussion

To date, many constitutive theories aimed at predicting the hyperelastic anisotropic behaviour of human AA and AAA have been proposed. A large number of them are built up within the framework of nonlinear continuum mechanics, and attempt to integrate information on tissue composition and internal structure. Therefore, recent constitutive laws are based on a purely phenomenological description (Vande Geest et al., 2006), or, most often, on a structurally motivated

Table 3 – Relative error between optimised data and experimental data depicted in Fig. 6, **mimicking experimental tension ratios $T_{\theta\theta} : T_{ll}$ for case AA (*left*) and case AAA (*right*). Maximum value $\epsilon_{\max}$, mean value $\bar{\epsilon}$. All errors are in %, as defined in Eq.** (8).

		Case AA		Case AAA	
	$T_{\theta\theta} : T_{ll}$	$\epsilon_{\max}$ (%)	$\bar{\epsilon}$ (%)	$\epsilon_{\max}$ (%)	$\bar{\epsilon}$ (%)
	0.5:1	60.17	18.88	92.21	28.75
	0.75:1	24.87	4.38	22.31	5.68
$\theta\theta$	1:1	5.12	1.55	7.52	6.00
	1:0.75	2.53	1.44	3.40	2.31
	1:0.5	10.74	4.53	7.69	2.08
	0.5:1	19.53	4.35	10.26	5.26
	0.75:1	2.92	1.16	3.87	2.72
ll	1:1	8.95	1.25	11.09	3.05
	1:0.75	26.56	4.98	20.90	6.43
	1:0.5	78.66	21.78	44.46	10.67

approach inspired from histological evidence (Gasser et al., 2006; Rodriguez et al., 2008; Basciano and Kleinstreuer, 2009; Ferruzzi et al., 2011). Doing so, anisotropy can thus be formulated by including either a finite number of collagen fibre preferred directions (Holzapfel et al., 2000, 2002; Basciano and Kleinstreuer, 2009; Ferruzzi et al., 2011) or a continuous distribution accounting for fibre dispersion (Zulliger et al., 2004; Driessen et al., 2004; Gasser et al., 2006; Ehret and Itskov, 2007; Rodriguez et al., 2008). These prior descriptions have allowed important computational advances on fluid/structure interactions and recently demonstrated the strong influence of the material anisotropy in the numerical prediction of AAA risk of rupture (Rodriguez et al., 2008; Rissland et al., 2009; Toungara et al., 2012). Nevertheless, despite their ability to capture the typical macroscopic
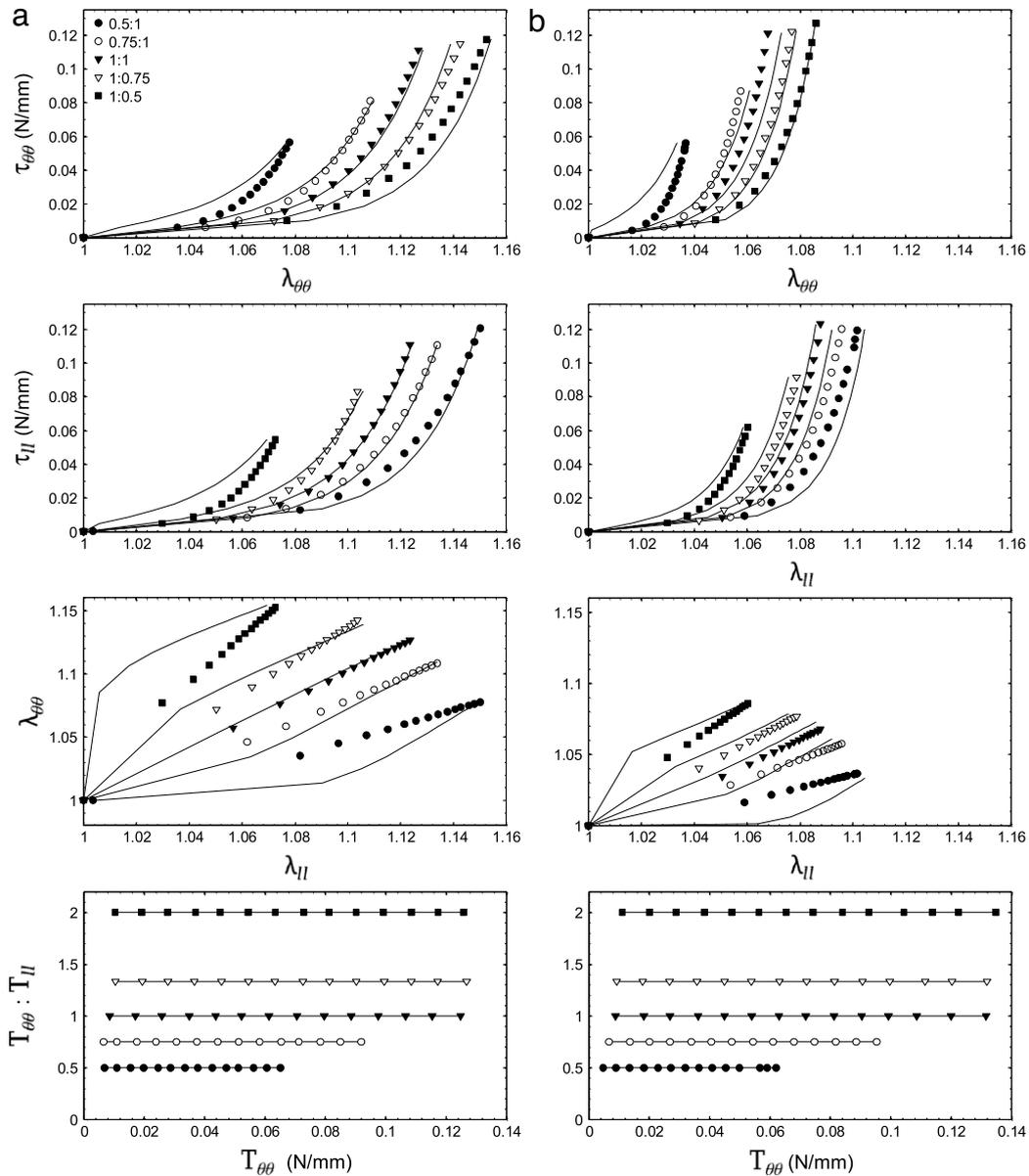
Fig. 6 – Comparison between the predictions of the *bi-layer* model (solid lines) and Vande Geest experimental data (symbols) at the macroscopic scale for (a) AA and (b) AAA samples. Optimisation has been processed as an average on the five investigated bi-axial loads. Optimised data are displayed here while imposing experimental Piola–Kirchhoff tension ratios $T_{\theta\theta} : T_{ll}$.

Table 4 – Optimised microstructural parameters of the bi-layer composite material, obtained for optimisations run firstly on both extreme ratios $T_{\theta\theta} : T_{ll}$, then on all five experimental bi-axial loads.

	Case AA				Case AAA			
$T_{\theta\theta} : T_{ll}$	$\tilde{c}_0$ (N mm^{-1}) $\times 10^{-4}$	c_1 (−)	θ_0^I(°)	θ_0^{II}(°)	$\tilde{c}_0$ (N mm^{-1}) $\times 10^{-4}$	c_1 (−)	θ_0^I(°)	θ_0^{II}(°)
0.5:1 & 1:0.5	2.99	37.00	30	61	1.47	70.37	27	58
All	2.80	37.99	31	60	1.53	70.73	27	56

features of the arterial wall mechanics, existing constitutive theories are not suitable to design a new composite fibre-reinforced phantom of the aortic tissue. For that purpose, we have proposed in this study an original approach elaborated

by means of a homogenisation technique applied to periodic discrete media coupled with an optimisation process, which allow the control of the macroscopic anisotropy by the fibre arrangement, geometry and mechanical behaviour.

In this specific theoretical framework, we have shown that a simple *bi-layers solution* constituted by two parallel lattices of equivalent fibres was necessary to mimic the major hyperelastic anisotropic properties of healthy and aneurysmal aortic tissues. An ideal microstructure has been identified on the average experimental data carried out by Vande Geest et al. (2006). This is discussed hereafter.

4.1. Optimal fibre architecture

The macroscopic anisotropy of the healthy AA tissue is optimally captured by the *bi-layers solution*, if defined by two parallel fibre lattices respectively orientated by $\pm 31°$ and $\pm 60°$ from the artery orthoradial direction in the stress-free state. These results remain unchanged when modifying the other geometrical specifics of both fibrous networks, such as fibre lengths, tortuosities or cross-sections. This optimal architecture is in quantitative agreement with the (sparse) observations made by inspection of human AA histological sections (Holzapfel et al., 2002; Holzapfel, 2006; Horny et al., 2010). In particular, statistical analyses presented in Holzapfel (2006) led to mean collagen fibre angles of about $\pm 20°, \pm 38°$ and $\pm 59°$ in *intimal*, *medial* and *adventitial* strips of an AA specimen excised on a human cadaver (female, 80 years-old, primary disease: congestive cardiomyopathy). These results were obtained by assuming a normal distribution and symmetrical arrangement with respect to the orthoradial direction. More recently, Horny et al. (2010) have analysed histological sections obtained from abdominal aorta *media* of a 36 year-old male donor and measured a continuous density distribution of collagen fibre orientations, with a density peak located nearly $30°$ (absolute value). Both collagen and SMC nuclei analysis revealed density maxima between $[20°; 50°]$. All these histological data have been reported in Fig. 7, together with the preferred fibre orientations identified in the present work, after both individual and mean optimisation procedures. This figure supports the assumption that the *bi-layers solution* tends to mimic the microstructural arrangement of both the *medial* and *adventitial* layers, so as to behave mechanically with the appropriate anisotropy at the macroscale.

This hypothesis is reinforced in the light of the five individual optimisations output, which were preliminary run with the *one-layer solution* (see Fig. 7). Indeed, the latter demonstrated that an angle θ_0^I below $45°$ was needed to mimic stress–elongation curves measured at a bi-axial loadings such as $T_{\theta\theta} : T_{ll} > 1$, whereas an angle θ_0^I above $45°$ was necessary to mimic stress–elongation curves when $T_{\theta\theta} : T_{ll} < 1$. This can explain why two degrees of freedom, i.e. $\theta_0^I < 45°$ and $\theta_0^{II} > 45°$, are the least required by the homogenised model to predict the different macroscopic responses measured at inverse bi-axial loadings $T_{\theta\theta} : T_{ll} = \alpha$ and $T_{\theta\theta} : T_{ll} = 1/\alpha$ (α being an arbitrary ratio, $\alpha \neq 1$). This feature is consistent with the layer-specific properties of arterial tissue, as identified by Holzapfel et al. (2005) in the case of human coronary arteries. In this study, individual *medial* and *adventitial* strips were subjected to cyclic quasi-static uniaxial tensile tests in the longitudinal and orthoradial directions. Interestingly, *adventitia* samples orientated in the longitudinal direction exhibited a tendency to be stiffer than
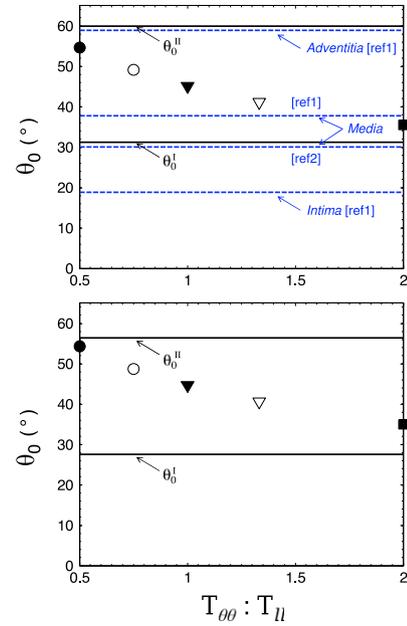
Fig. 7 – Comparison between the fibre orientations θ_0^I predicted by the *one-layer* model (individual optimisations, *symbols*), θ_0^I and θ_0^{II} predicted by the *bi-layer* model (mean optimisation on the five experimental loading paths, *solid lines*), and histological data reported by Holzapfel (2006) [ref1] and Horny et al. (2010) [ref2] (*dashed lines*). (top) AA case, (bottom) AAA case.

the corresponding samples in the orthoradial direction (thus requiring $\theta_0^{II} > 45°$ in our modelling), whereas the opposite was observed for the *media* samples (thus requiring $\theta_0^I < 45°$). Therefore, although the *media* is commonly referred as the main mechanically relevant arterial layer, our results suggest instead that both *media* and *adventitia* layers should be of greater importance to generate a relevant macroscopic arterial anisotropy in response to (non-equi) bi-axial loadings.

Consequently, according to the present modelling assumptions, a composite material that was limited to a single preferred fibre orientation could not reproduce the intended anisotropic behaviour evidenced for two inverse ratios $T_{\theta\theta} : T_{ll} = \alpha$ and $T_{\theta\theta} : T_{ll} = 1/\alpha$ ($\alpha \neq 1$). In particular, a $\pm 45°$ fibre-orientation in the one-layer model (mimicking the *media*-layer mechanical contribution alone) would not be able to predict any of the relevant anisotropic effects typically observed in aortic mechanics, as illustrated in Fig. 5. This feature clearly contrasts with the predictions of previous phenomenological approaches such as the two-fibre family model proposed by Basciano and Kleinstreuer (2009), where the angle value does not have the same immediate physical interpretability (see Fig. 3 therein).

4.2. Optimal fibre mechanical behaviour

Together with the fibre orientations, an optimal microscopic tension per unit of length $\bar{t}(\lambda)$ has been found from the adjustment on the bi-axial mechanical data, allowing multiple available choices for the last couple $(t(\lambda), l_0)$ to be determined. Several technical solutions can be imagined in

order to satisfy the optimised function $\tilde{t}(\lambda)$: single straight fibres, single wavy fibres, complex straight or wavy yarns.... In what follows, the two first solutions are considered.

4.2.1. Straight fibres

We first consider that the lattice consists in using straight fibres of initial diameter d_0^f and initial length l_0^f. Under the incompressibility assumption (here stated for simplicity), tension $\tilde{t}$ is a function of the fibre initial cross-section S_0^f, initial length l_0^f, stretch λ and Cauchy stress σ^f, so that $\tilde{t} = (S_0^f \sigma^f)/(l_0^f \lambda^2)$. Therefore, the optimisation output remains unchanged when modifying the triplet (S_0^f, l_0^f, σ^f), provided that the latter relation is conserved. Hence, depending on the microstructure and constitutive parameters (S_0^f, l_0^f, σ^f), various types of fibre mechanical behaviours are potentially good candidates to constitute the optimised fibrous lattices. To better illustrate this, we have plotted in Fig. 8 the available mechanical behaviour of the fibre bulk material, i.e. $\sigma^f(\lambda)$, for various fibre lengths l_0^f and diameters d_0^f. In particular, by considering a length l_0^f between 1 to 10 mm and a diameter fixed at $d_0^f = 0.15$ mm (Fig. 8(a)), the optimal materials display an elastic modulus E_c ranging from 69 to 689 MPa in the healthy case, and from 111 to 1115 MPa in the pathological case at $\lambda = \tilde{\lambda}_c$, as assessed in Section 3.2. These moduli rise from 315 to 3151 MPa in the healthy case, and from 422 to 4221 MPa in the pathological case, if evaluated at the end of the loads. Notice that this point is of primary interest prior to the material manufacturing step, by covering a wide choice of microstructural parameters that could help solving potential technological constraints. Nevertheless, due to the high non-linearity of the adjusted microstructural mechanical behaviour (typical J-shape curve), the selection of appropriate monofilament candidates constitutes a challenging task, which could not be achieved using usual metal, ceramic or polymer fibres. Indeed, the latter are characterised by linear elastic stress–strain responses over the concerned stress range. Even polymeric or metallic materials which exhibit a non-linear reversible mechanical behaviour such as elastomers or shape memory alloys (SMAs) could hardly be suitable to reproduce the target J-shape response under this manufacturing solution (i.e. bulk monofilaments of technically feasible diameters). In particular, superelastic SMAs are characterised by a rather low stress-induced martensitic transformation elongation (≈ 1.05 in tension) as compared to the critical elongation $\tilde{\lambda}_c$ identified in case AA (≈ 1.11). Also, before exhibiting a J-shape-like response, SMAs display an initial elastic domain up to very high stress levels (≈ 500 MPa) (Orgéas and Favier, 1998; Otsuka and Ren, 2005; Barney et al., 2011). As to bulk elastomers, their critical elongation is typically found to be over 1.50, that is, far beyond the target one (Meunier et al., 2008).

4.2.2. Wavy fibres

We consider now another interesting and simple solution, i.e. a lattice which is made up of elastic wavy fibres of Young modulus E^f, initial diameter d_0^f, initial length l_0^f, initial tortuosity $\xi_0 = l_0^f/l_0$ and initial curvature along its curvilinear abscissa s, $\kappa_0^f(s)$ (see Fig. 9). The mechanical response of such curved fibres, when stretched at their extremities,
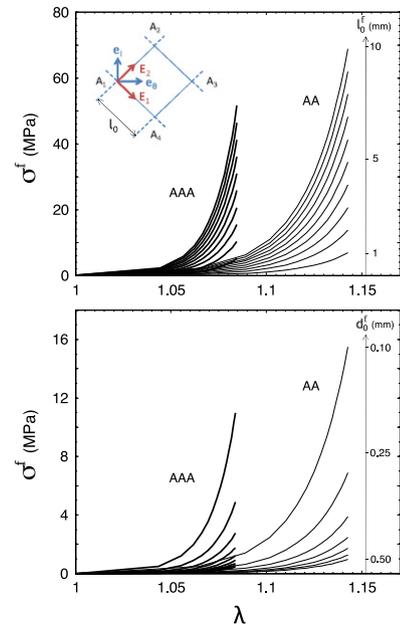
Fig. 8 – Influence of the microstructure parameters on the optimised mechanical behaviour of the fibre as predicted by the bi-layer model. Influence of (top) fibre length l_0^f, varied between 1 and 10 mm with fixed $d_0^f = 0.15$ mm; (bottom) fibre diameter d_0^f, varied between 0.10 and 0.50 mm with fixed $l_0^f = 1$ mm. One of the two lattices (REC) is sketched in the upper graph.
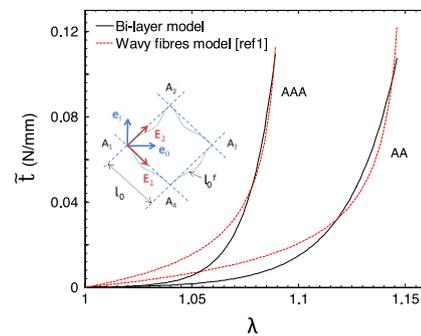
Fig. 9 – Comparison between the optimised microscopic mechanical behaviour $\tilde{t} - \lambda$ predicted by the bi-layer model and that predicted by the wavy fibres model described in Kabla and Mahadevan (2007) [ref1], with lattice length $l_0 = 2$ mm, fibre stiffness $B = 0.0085$ MPa mm^4 and an optimised value of fibre length l_0^f (2.30 mm for the AA case and 2.19 mm for AAA case). One of the two lattices (REC) is sketched in the graph.

is dominated by the unbending of the initially curved regions, at least until the fibres become nearly straight. By assuming that fibres are inextensible (a reasonable assumption until the fibres are nearly straight), Kabla and Mahadevan (2007) have shown that the fibre tortuosity $\xi = l^f/l$ could be related to the tension t by the following analytical

expression:

$$\frac{1}{\xi} = \lambda \frac{1}{\xi_0} = 1 - \sum_k \frac{A_k^2 k^2}{4\left(\frac{t}{B} + k^2\right)^2}, \qquad (9)$$

which is valid for a initial tortuosity ξ_0 (*i.e.* when $t = 0$) below 1.18. In this expression, $B = E^f \pi d_0^{f\,4}/64$ is the bending stiffness, A_k and k are parameters which characterise the amplitude and the wavelength of the curvature spectrum: $\kappa_0^f = \sum_k A_k \cos(ks + \phi_k)$, $k = 2\pi n/l_0^f$, $n \in \mathbb{N}$. In the present work, the above relation was adjusted on the microscopic tension t versus λ curves in the particular case where $n = 1$ and $\phi_k = 0$. Therefore, the tension $t(\lambda)$ can be determined knowing three parameters only: the initial length of the lattice l_0 (or the initial tortuosity ξ_0 of the fibres), the initial fibre length l_0^f and the bending stiffness B. The lattice parameter l_0 was set to a representative value of 2 mm and the stiffness B was fixed to 0.0085 MPa mm^4. Obviously, this bending stiffness can be achieved using different potential couples (d_0^f, E^f). In particular, the same value is obtained using linear elastic metal, ceramic or polymer monofilaments, such as steel wires (30 μm, 200 GPa), glass fibres (40 μm, 70 GPa) or fluorocarbon fibres commonly used as fishing wires (0.10 mm, 2000 MPa) for instance. An illustrative adjustment of Eq. (9) on microscopic tension $t(\lambda)$ has been performed under such assumptions. This is illustrated in Fig. 9, showing that these types of wavy fibre could be good candidates: a rather good agreement is obtained for the AA and AAA cases (this was obtained by considering an optimal fibre length l_0^f of 2.30 mm and 2.19 mm, respectively).

5. Conclusion and future work

The objective of this study was to propose a new theoretical framework, devoted to create a new material model mimicking the hyperelastic anisotropic properties of healthy and aneurysmal abdominal aortic tissue. A first attempt characterised by a simple microstructure and using an original homogenisation method has been proposed. Average bi-axial tensile data carried out by Vande Geest et al. (2006) have been chosen as a reference to identify the mechanical behaviour of the biological tissue at the macroscopic scale. Two theoretical models have been optimised on five bi-axial tension ratios, representative of the loading in aortic tissue: a one-layer model comprising a single fibre lattice embedded into an elastomeric matrix, and a bi-layer model constituted by two mechanically equivalent fibre lattices. It was first shown that a composite constituted by only a single lattice of fibres was not sufficient to describe all the experimental data, whereas a quantitative agreement between measurements and theoretical predictions was obtained by using the bi-layer model. This bi-layer model depends on five parameters only, four of them are related to the fibrous lattices $(\theta_0^I, \theta_0^{II}, \tilde{c}_0, c_1)$, the last one is related to the elastomeric matrix $(c^m e_0^m)$. An ideal microstructural architecture and optimal fibre mechanical behaviours have been proposed, which provide a new insight into the structural mechanisms underlying the anisotropic behaviour of the aorta. In future work, the

microstructural parameter dependency with gender and age should be identified on patient-specific data and compared to predictions of previous phenomenological models. Searching for appropriate fibre and matrix candidates corresponding to the adjusted microstructure is the next challenging task. Regarding the matrix, standard silicone elastomers could be relevant candidates, for example. Regarding the fibrous structure which governs the overall mechanical behaviour of the considered composite membranes, we have shown that the use of bulk and straight monofilaments was hardly conceivable using either linear elastic metal, ceramic or polymer materials, or even elastomers or memory shape alloys. However, the use of composite fibres could be a relevant way to overcome this difficulty. Also, this study demonstrated that linear elastic materials may however be used provided a proper fibrous architecture is considered, such as a wavy substructure for instance. In light of this work, more complex wavy yarns could also be envisaged as a further successful technical solution. Finally, experimental tests on composite material samples will be conducted in order to validate the different model assumptions.

REFERENCES

Barney, M.M., Xu, D., Robertson, S.W., Schroeder, V., Ritchie, R.O., Pelton, A.R., Mehta, A., 2011. Impact of thermomechanical texture on the superelastic response of Nitinol implants. Journal of the Mechanical Behavior of Biomedical Materials 4, 1431–1439.

Basciano, C.A., Kleinstreuer, C., 2009. Invariant-based anisotropic constitutive models of the healthy and aneurysmal abdominal aortic wall. Journal of Biomechanical Engineering 131 (1), 021009/1–021009/11.

Boland, E., Matthews, J.A., Pawlowski, K.J., Simpson, D.G., Wnek, G.E., Bowlin, G.L., 2004. Electrospinning collagen and elastin: preliminary vascular tissue engineering. Frontiers in Bioscience 9, 1422–1432.

Boutin, C., Hans, S., 2003. Homogenisation of periodic discrete medium: application to dynamics framed structures. Computers and Geotechnics 30, 303–320.

Byrd, R.H., Gilbert, J.C., Nocedal, J., 2000. A trust region method based on interior point techniques for nonlinear programming. Mathematical Programming 89 (1), 149–185.

Caillerie, D., Mourad, A., Raoult, A., 2006. Discrete homogenization in graphene sheet modeling. Journal of Elasticity 84 (1), 33–68.

Chakfe, N., Dieval, F., Riepe, G., Mathieu, D., Zbali, I., Thaveau, F., Heintz, C., Kretz, J., Durand, B., 2004. Influence of the textile structure on the degradation of explanted aortic endoprostheses. European Journal of Vascular and Endovascular Surgery 27, 33–41.

Chong, C.K., How, T.V., 2004. Flow patterns in an endovascular stent-graft for abdominal aortic aneurysm repair. Journal of Biomechanics 37, 89–97.

Deplano, V., Knapp, Y., Bertrand, E., Gaillard, E., 2007. Flow behaviour in an asymmetric compliant experimental model for abdominal aortic aneurysm. Journal of Biomechanics 40, 2406–2413.

Dobrin, P.B., 1978. Mechanical properties of arteries. Physiological Reviews 58 (2), 397–460.

Doyle, B.J., Cloonan, A.J., Walsh, M.T., Vorp, D.A., McGloughlin, T.M., 2010. Identification of rupture locations in patient-specific abdominal aortic aneurysms using experimental and computational techniques. Journal of Biomechanics 43 (7), 1408–1416.

Driessen, N.J.B., Wilson, W., Bouten, C.V.C., Baaijens, F.P.T., 2004. A computational model for collagen fibre remodelling in the arterial wall. Journal of Theoretical Biology 226, 53–64.

Egelhoff, C., Budwig, R., Elger, D., Khraishi, T., Johansen, K., 1999. Model studies of the flow in abdominal aortic aneurysms during resting and exercise conditions. Journal of Biomechanics 32, 1319–1329.

Ehret, A.E., Itskov, M., 2007. A polyconvex hyperelastic model for fiber-reinforced materials in application to soft tissues. Journal of Materials Science 42, 8853–8863.

Ferruzzi, J., Vorp, D.A., Humphrey, J.D., 2011. On constitutive descriptors of the biaxial mechanical behaviour of human abdominal aorta and aneurysms. Journal of the Royal Society Interface 8, 435–450.

Freed, A.D., Einstein, D.E., Vesely, I., 2005. Invariant formulation for dispersed transverse isotropy in aortic heart valves: an efficient means for modeling fiber splay. Biomechanics and Modeling in Mechanobiology 4, 100–117.

Gasser, T.C., Ogden, R.W., Holzapfel, G.H., 2006. Hyperelastic modelling of arterial layers with distributed collagen fibre orientations. Journal of the Royal Society Interface 3, 15–35.

He, C.M., Roach, M.R., 1994. The composition and mechanical properties of abdominal aortic aneurysms. Journal of Vascular Surgery 20, 6–13.

Holzapfel, G., 2006. Determination of material models for arterial walls from uniaxial extension tests and histological structure. Journal of Theoretical Biology 238, 290–302.

Holzapfel, G.A., 2008. Collagen in Arterial Walls: Biomechanical Aspects. Springer-Verlag, pp. 285–324 (Chapter 11).

Holzapfel, G.A., Gasser, T.C., Ogden, R.W., 2000. A new constitutive framework for arterial wall mechanics and a comparative study of material models. Journal of Elasticity 61, 1–48.

Holzapfel, G., Gasser, T., Stadler, M., 2002. A structural model for the viscoelastic behavior of arterial walls: continuum formulation and finite element analysis. European Journal of Mechanics A/Solids 21, 441–463.

Holzapfel, G., Sommer, G., Gasser, C.T., Regitnig, P., 2005. Determination of layer-specific mechanical properties of human coronary arteries with nonatherosclerotic intimal thickening and related constitutive modeling. American Journal of Physiology—Heart and Circulatory Physiology 289, 2048–2058.

Horny, L., Kronek, J., Chlup, H., Zitny, R., Vesely, J., Hulan, M., 2010. Orientations of collagen fibers in aortic histological section. Bulletin of Applied Mechanics 6 (22), 25–29.

Humphrey, J.D., Na, S., 2002. Elastodynamics and arterial wall stress. Annals of Biomedical Engineering 30, 509–523.

Humphrey, J., Taylor, C., 2008. Intracranial and abdominal aortic aneurysms: Similarities, differences, and need for a new class of computational models. Annual Review of Biomedical Engineering 10, 221–246.

Jacobs, T., Won, J., Gravereaux, E.C., Faries, P.L., Morrissey, N., Teodorescu, V.J., Hollier, L.H., Marin, M., 2003. Mechanical failure of prosthetic human implants: a 10-year experience with aortic stent graft devices. Journal of Vascular Surgery 37, 16–26.

Kabla, A., Mahadevan, L., 2007. Nonlinear mechanics of soft fibrous networks. Journal of the Royal Society Interface 4, 99–106.

Kleinstreuer, C., Li, Z., Farber, M., 2007. Fluid–structure interaction analyses of stented abdominal aortic aneurysms. Annual Review of Biomedical Engineering 9, 169–204.

Kuhn, H.W., Tucker, A.W., 1951. Nonlinear Programming. University of California Press, pp. 481–492.

Lasheras, J.C., 2007. The biomechanics of arterial aneurysms. The Annual Review of Fluid Mechanics 39, 293–319.

Le Corre, S., Caillerie, D., Orgéas, L., Favier, D., 2004. Behavior of a net of fibers linked by viscous interactions: theory and mechanical properties. Journal of the Mechanics and Physics of Solids 52, 395–421.

McClure, M., Sell, S., Simpson, D., Walpoth, B.H., Bowlin, G.L., 2010. A three-layered electrospun matrix to mimic native arterial architecture using polycaprolactone, elastin, and collagen: a preliminary study. Acta Biomaterialia 6, 2422–2433.

Meunier, L., Chagnon, G., Favier, D., Orgéas, L., Vacher, P., 2008. Mechanical experimental characterisation and numerical modelling of an unfilled silicone rubber. Polymer Testing 27, 765–777.

Nocedal, J., Wright, S.J., 2006. Numerical Optimization, second ed. Springer Verlag.

Orgéas, L., Favier, D., 1998. Stress-induced martensitic transformation of a NiTi alloy in isothermal shear, tension and compression. Acta Materialia 46, 5579–5591.

Otsuka, K., Ren, X., 2005. Physical metallurgy of Ti–Ni-based shape memory alloys. Progress in Materials Science 50, 511–678.

Raghavan, M.L., Kratzberg, J., de Tolosa, E.M.C., Hanaoka, M.M., Walker, P., da Silva, E.S., 2006. Regional distribution of wall thickness and failure properties of human abdominal aortic aneurysm. Journal of Biomechanics 39, 3010–3016.

Raghavan, M.L., Webster, M.W., Vorp, D.A., 1996. Ex vivo biomechanical behavior of abdominal aortic aneurysm: Assessment using a new mathematical model. Annals of Biomedical Engineering 24, 573–582.

Rissland, P., Alemu, Y., Einav, S., Ricotta, J., Bluestein, D., 2009. Abdominal aortic aneurysm risk of rupture: patient-specific FSI simulations using anisotropic model. Journal of Biomechanical Engineering 131, 1–10.

Rodriguez, J., Ruiz, C., Doblaré, M., Holzapfel, G.A., 2008. Mechanical stresses in abdominal aortic aneurysm: influence of diameter, asymmetry, and material anisotropy. Journal of Biomechanical Engineering 130, 1–10.

Salsac, A.-V., Sparks, S., Chomaz, J., Lasheras, J., 2006. Evolution of the wall shear stresses during the progressive enlargement of symmetric abdominal aortic aneurysms. Journal of Fluid Mechanics 560, 19–51.

Scotti, C.M., Finol, E.A., 2007. Compliant biomechanics of abdominal aortic aneurysms: a fluid–structure interaction study. Computers and Structures 85, 1097–1113.

Thubrikar, M.J., Labrosse, M., Robicsek, F., Al-Soudi, J., Fowler, B., 2001. Mechanical properties of abdominal aortic aneurysm wall. Journal of Medical Engineering and Technology 25, 133–142.

Tollenaere, H., Caillerie, D., 1998. Continuous modeling of lattice structures by homogenization. Advances in Engineering Software 29 (7), 699–705.

Toungara, M., Chagnon, G., Geindreau, C., 2012. Numerical analysis of the wall stress in abdominal aortic aneurysm: influence of the material model near-incompressibility. Journal of Mechanics in Medicine and Biology http://dx.doi.org/10.1142/S0219519412004442.

Valenta, J., 1993. Biomechanics. In: Clinical Aspects of Biomedicine, vol. 2. Elsevier, New York, pp. 150–164. (Chapter).

Vande Geest, J.P., Sacks, M.S., Vorp, D.A., 2004. Age dependency of the biaxial biomechanical behavior of human abdominal aorta. Journal of Biomechanical Engineering 126, 815–822.

Vande Geest, J.P., Sacks, M.S., Vorp, D.A., 2006. The effects of aneurysm on the biaxial mechanical behavior of human abdominal aorta. Journal of Biomechanics 39, 1324–1334.

Vande Geest, J.P., Schmidt, D.E., Sacks, M.S., Vorp, D.A., 2008. The effects of anisotropy on the stress analyses of patient-specific abdominal aortic aneurysms. Annals of Biomedical Engineering 36, 921–932.

VanLieshout, M., Vaz, C., Rutten, M., Peters, G., Baaijens, F., 2006. Electrospinning versus knitting: two scaffolds for tissue engineering of the aortic valve. Journal of Biomaterials Science, Polymer 17, 77–78.

Volokh, K., 2008. Prediction of arterial failure based on a microstructural bi-layer fiber-matrix model with softening. Journal of Biomechanics 41 (2), 447–453.

Vorp, D.A., Geest, J.P.V., 2005. Biomechanical determinants of abdominal aortic aneurysm rupture. Arteriosclerosis, Thrombosis, and Vascular Biology 25, 1558–1566.

Waltz, R.A., Morales, J.L., Nocedal, J, Orban, D., 2006. An interior algorithm for nonlinear optimization that combines line search and trust region steps. Mathematical Programming 107 (3), 391–408.

Wolinsky, H., Glagov, S., 1964. Structural basis for the static mechanical properties of the aortic media. Circulation Research 13, 400–413.

Wolters, B., Rutten, M., Schurink, G., Kose, U., de Hart, J., van de Vosse, F., 2005. A patient-specific computational model of fluid–structure interaction in abdominal aortic aneurysms. Medical Engineering and Physics 27, 871–883.

Zulliger, M.A., Fridez, P., Hayashi, K., Stergiopulos, N., 2004. A strain energy function for arteries accounting for wall composition and structure. Journal of Biomechanics 37, 989–1000.